communications biology

Article

https://doi.org/10.1038/s42003-024-06846-7

Atoh1 mediated disturbance of neuronal maturation by perinatal hypoxia induces cognitive deficits

Check for updates

Xin-yu Cai [1,3], Si-yu Ma [1,3] ✉, Ming-hui Tang [1,3], Liang Hu [1], Ke-de Wu [1], Zhen Zhang [1], Ya-qi Zhang [1], Ye Lin [1], Nishant Patel [1], Zhao-cong Yang [1] & Xu-ming Mo [1,2] ✉

Neurodevelopmental disorders are currently one of the major complications faced by patients with congenital heart disease (CHD). Chronic hypoxia in the prenatal and postnatal preoperative brain may be associated with neurological damage and impaired long-term cognitive function, but the exact mechanisms are unknown. In this study, we find that delayed neuronal migration and impaired synaptic development are attributed to altered Atoh1 under chronic hypoxia. This is due to the fact that excessive Atoh1 facilitates expression of Kif21b, which causes excess in free-state α-tubulin, leading to disrupted microtubule dynamic stability. Furthermore, the delay in neonatal brain maturation induces cognitive disabilities in adult mice. Then, by down-regulating *Atoh1* we alleviate the impairment of cell migration and synaptic development, improving the cognitive behavior of mice to some extent. Taken together, our work unveil that *Atoh1* may be one of the targets to ameliorate hypoxia-induced neurodevelopmental disabilities and cognitive impairment in CHD.

Congenital heart disease (CHD) is one of the most common birth's defects[1]. With advances in surgical technique, patients are surviving longer nowadays[2]. However, numerous extra-cardiac complications have made CHD a life-long chronic condition. Among them, neurodevelopmental disabilities are one of the typical life-long complicating diseases[3]. Cyanotic congenital heart disease (CCHD) is one of the complex and critical CHD forms. It has been shown that neurodevelopmental deficits can be as high as 50% in patients with CCHD[4,5], which can persist into adolescence and adulthood followed up over time[6,7]. However, there are few effective interventions for neurologic complications in patients with CCHD at the present time.

Chronic hypoxia during the prenatal and postnatal preoperative periods, which overlap with critical periods of brain development, is a typical feature of patients with CCHD[8]. Low oxygen saturation in the brains of fetuses and neonates with CCHD after magnetic resonance imaging (MRI) testing showed strong association with abnormal structural brain development[8,9]. At the same time, inadequate oxygen and nutrient delivery to the brain caused by abnormal fetal circulation of children with CCHD might also contribute to delayed brain development prior to corrective surgery[10]. In previous work, we uncovered that the lack of oxygen in the brain continued to affect the cognitive function of children with CCHD at least until the pre-school period[11,12]. Therefore, in addition to timely postnatal surgical correction, the specific mechanisms underlying the neurodevelopmental deficits and cognitive impairments associated with chronic hypoxia in CCHD need to be investigated in depth to provide a theoretical basis for the search for preoperative targets to protect the brain in patients.

Transcription factors (TFs) are involved in several vital developmental processes such as neuronal proliferation, migration, and differentiation in the central nervous system (CNS). Under oxygen supply pressure, alterations of TFs would cause a series of changes in cellular downstream signaling[13,14]. However, there are few studies on the role of TFs in the development of neonatal brain under chronic hypoxia nowadays. Since we found that many TFs altered in chronic hypoxic mice brains, including *Atoh1*, a basic helix-helix TF which is widely distributed in the CNS[15,16], whose mutation caused deficits in retrotrapezoid nucleus neuronal migration[17], pontine nucleus differentiation[18], and cerebellar development with consequent motor disorders[19]. In addition, it has also been shown that *Atoh1* can hinder the normal differentiation process of proliferating cells[20]. Then, the question arose of how *Atoh1* affects neuronal biology and mice behaviors under chronic hypoxia.

In this study, we possessed a hypoxic model in neonatal mice to mimic the chronic hypoxia that CCHD patients face in late pregnancy[21,22]. In this model, we observed changes in resting-state brain function and impaired cognitive function of mice. These changes may be attributed to delayed neuronal migration and impaired synaptic development. Moreover, we

[1]Department of Cardiothoracic Surgery, Children's Hospital of Nanjing Medical University, Nanjing, 210008, China. [2]Nanjing University, Nanjing, 210008, China. [3]These authors contributed equally: Xin-yu Cai, Si-yu Ma, Ming-hui Tang. ✉e-mail: pupil616312@163.com; mohsuming15@njmu.edu.cn

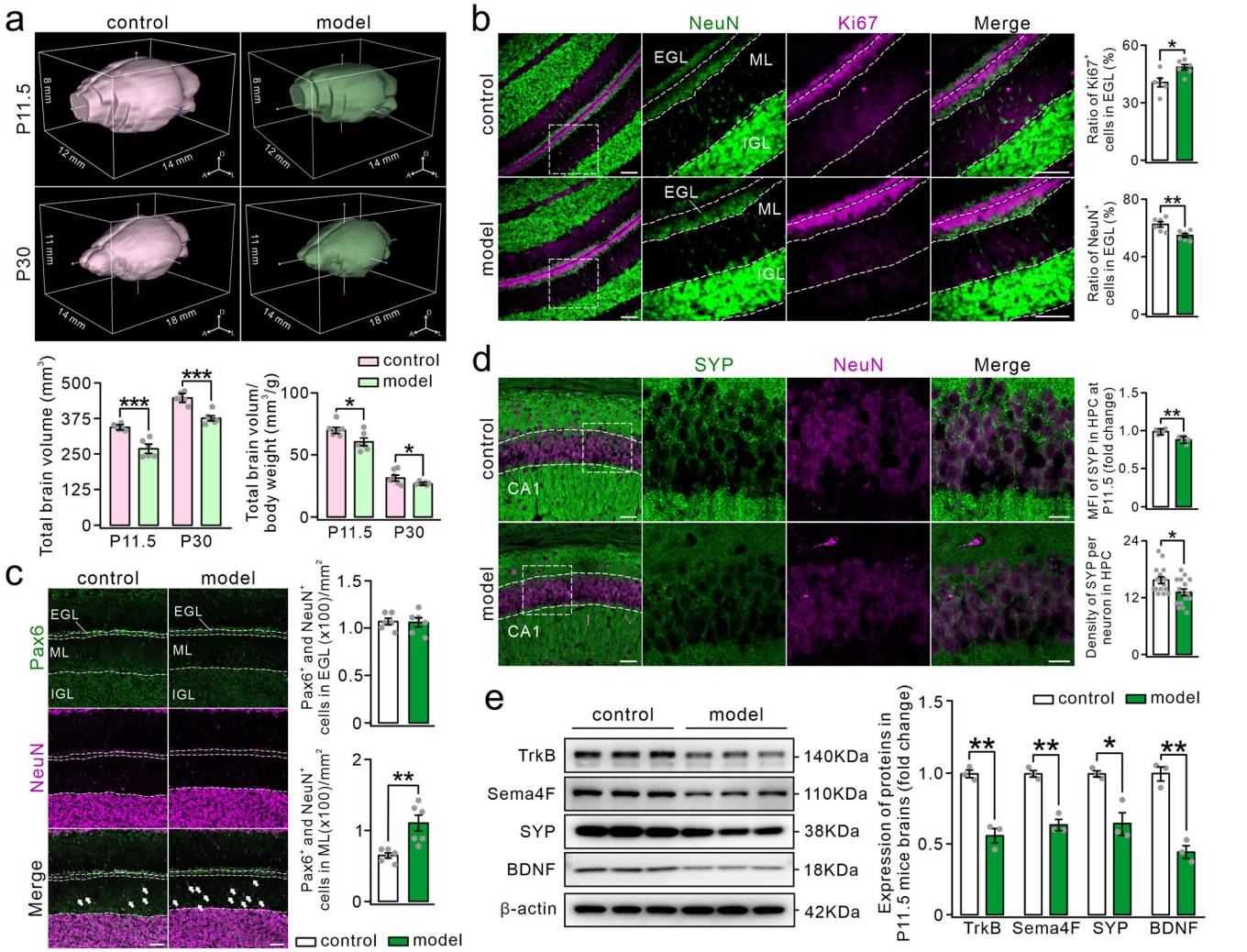

Fig. 1 | Structural aberration of brain after chronic hypoxia. a 3D graphs of control and model mice in P11.5 brain by T2 scanning (A, anterior; L, left; D, dorsal). Bar graphs on the left show the total brain volume of control and model mice at P11.5 and P30 (control, $n = 6$; model, $n = 6$) (For statistics, see Table S3). Bar graphs on the right show the normalized total brain volume of control and model mice at P11.5 and P30 (control, $n = 6$; model, $n = 6$) (For statistics, see Table S4). **b** Staining of cerebellar lobule IV-V by antibodies against Ki67 and NeuN in mice at P11.5. The three right panels show a magnified view of dashed squares on the left. (EGL, external granular layer; ML, molecular layer; IGL, internal granular layer) Scale bars: 50 μm. (column on the left, objective 20x; three right columns, objective 40x). Bar graph above shows the ratio of Ki67 positive cells in EGL. Bar graph below shows the ratio of NeuN positive cells in EGL (control, $n = 6$; model, $n = 6$) (For statistics, see Table S5). **c** Staining of cerebellar lobule III by antibodies against Pax6 and NeuN in mice at P11.5. Scale bars: 50 μm. Objective 20x. White arrows indicate double positive cells. Bar graph above shows the number of Pax6 and NeuN positive cells in EGL (control, $n = 6$; model, $n = 6$). Bar graph below shows the number of Pax6 and NeuN positive cells in ML (control, n = 6; model, n = 6) (For statistics, see Table S6). **d** Staining of hippocampal CA1 by antibodies against SYP and NeuN in mice at P11.5. The three right panel shows a magnified view of dashed squares on the left. HPC, hippocampus. Scale bars: 50 μm (columns on the left, objective 20x); 20 μm (three right columns, objective 63x). Bar graph above shows mean fluorescence intensity (MFI) of SYP staining, data were presented as relative to control (control, $n = 6$; model, $n = 6$). Bar graph below shows density of SYP$^+$ points on per neuron (control, $n = 16$; model, $n = 16$) (For statistics, see Table S7). **e** Protein fractions from brains of P11.5 mice were tested with TrkB, BDNF, SYP, and Sema4F. Left panels show representative bands of proteins mentioned above. β-actin was used as an internal control. Bar graphs on the right show percentage changes of proteins in model mice relative to control (control, $n = 3$; model, $n = 3$) (For statistics, see Table S8). All data were shown as mean ± SEM. $^*p < 0.05$, $^{**}p < 0.01$, $^{***}p < 0.001$.

exhibited that microtubule stability, which Atoh1/Kif21b is engaged in regulating, is closely in relation to the developmental processes above. The effects of hypoxia on neuronal development and cognitive functions can be moderately rescued by down-regulation of *Atoh1*. Collectively, these findings shed light on that Atoh1 under chronic hypoxia may hinder neurodevelopment by modulating Kif21b to constrain neuronal dendritic branching and cell migration by disrupting microtubules (MTs) dynamic stability.

Results

Chronic hypoxia disturbs neonatal brain maturation

The brain size of mice reared in the hypoxic environment was significantly diminished in P11.5 and P30 by MRI (Fig. 1a), while the brain volume of model mice was comparable with control mice at P60 (Fig. S1a). Since CCHD-associated long-term hypoxia can cause nutritional and developmental gap[23] (Fig. S1a), to exclude generalized developmental delay due to chronic hypoxia, we further standardized brain size by using the ratio of brain volume and body weight (V/W). V/W ratio also decreased in model mice both in P11.5 and P30 (Fig. 1a), but reverted at P60 (Fig. S1a), indicating that perinatal hypoxia shall especially lead to brain expansion delay before adulthood in mice. Neuronal migration and synapse formation are important in brain development and occur continually in late gestation and perinatal period[24,25]. On the basis of the immunofluorescence (IF), we demonstrated that the Ki67 positive cells at the outer external granular layer (EGL) increased while NeuN positive cells at the inner EGL decreased in the

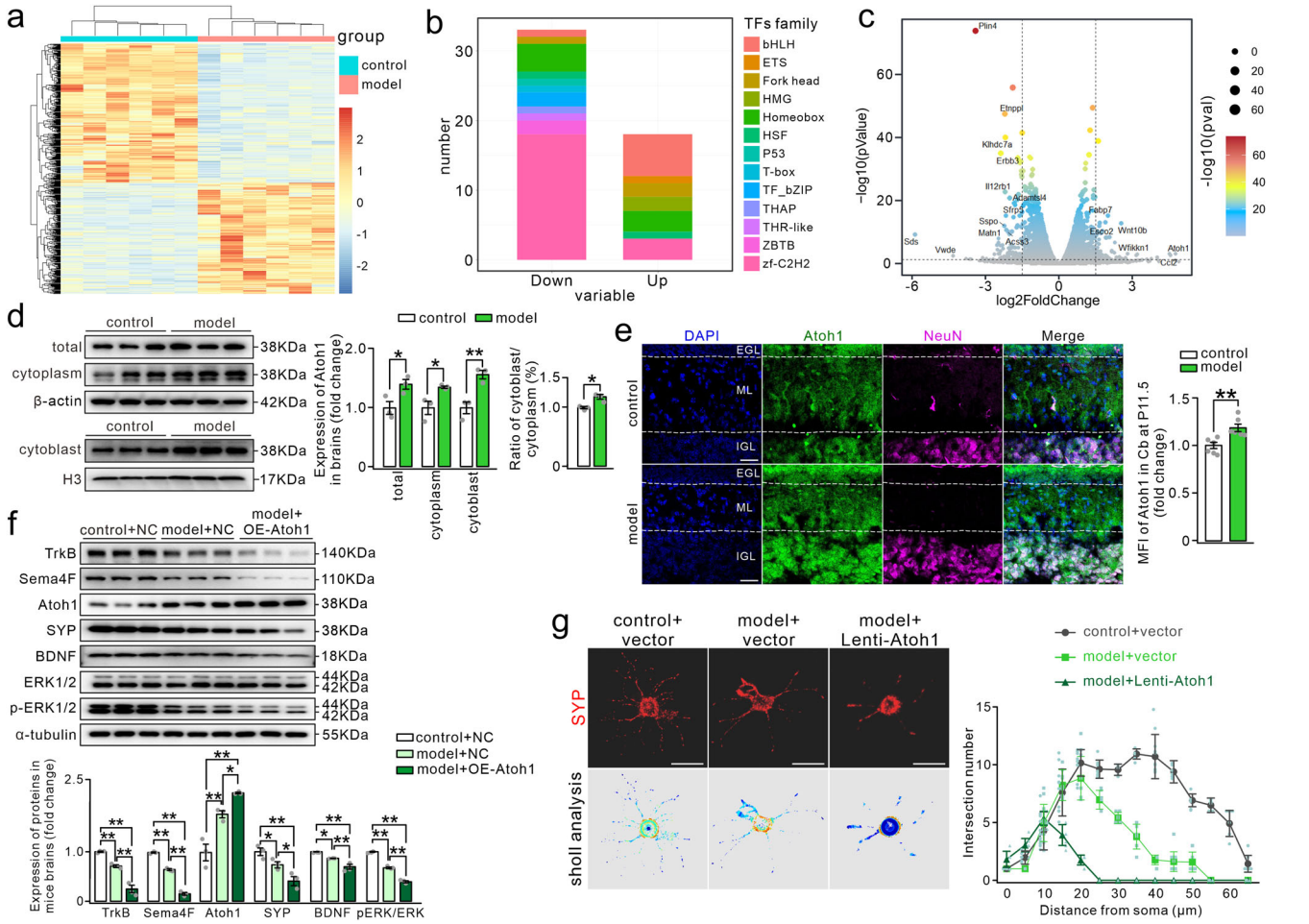

Fig. 2 | Altered Atoh1 levels in the hypoxic neonatal brain affected neuronal development. a Heat map shows DEGs of the whole brain from P11.5 mice (control, $n = 6$; model, $n = 6$) ($p < 0.05$, $Log_2FC > 1$). **b** Bar graph shows TFs families in DEGs (control, $n = 6$; model, $n = 6$) ($p < 0.05$, $Log_2FC > 1$). **c** Volcano plot shows genes in the leading positions of DEGs (control, $n = 6$; model, $n = 6$) ($p < 0.05$, $Log_2FC > 1.5$). **d** Protein fractions in cytoplasm and cytoblast extracted from P11.5 mice brains were tested with Atoh1. Left panels show representative bands of Atoh1. β-actin and H3 were used as internal controls of cytoplasm and cytoblast, respectively. Bar graphs on the left show percentage changes of proteins in model mice relative to control. Bar graph on the right shows ratio of Atoh1 level in cytoblast relative to cytoplasm. (control, $n = 3$; model, $n = 3$) (For statistics, see Table S9). **e** Staining of cerebellar lobule III by antibodies against Atoh1 and NeuN in P11.5 mice. Cb, cerebellum. Scale bars: 20 μm. Objective 40x. Bar graph shows MFI of Atoh1 staining (control, $n = 6$; model, $n = 6$) ($t = -3.89$, $^{**}p = 0.0030$, $df = 10$) (1.00 ± 0.033 vs 1.20 ± 0.040). **f** Protein fractions from P11.5 mice brains of control and model mice were tested with TrkB, BDNF, SYP, Sema4F, Atoh1, pErk1/2, and Erk1/2. Left panels show representative bands of proteins mentioned above. α-tubulin was used as an internal control. (NC, negative control; OE, over expression). Bar graphs show percentage changes of proteins (control + NC, $n = 3$; model + NC, $n = 3$; model + OE-Atoh1, $n = 3$) (For statistics, see Table S10). **g** Sholl analysis of cultured primary neurons stained of SYP. Left panels show representative staining of SYP and intersection of dendrites with concentric circles. Line chart shows the intersection numbers of dendrites and concentric circles. Scale bars: 20 μm. Objective 63x. (All groups, $n = 6$ batches for each group, $n = 2$ cells for each batch) (For statistics, see Table S11). All data were shown as mean ± SEM. $^{*}p < 0.05$, $^{**}p < 0.01$.

model mice (Fig. 1b), which is the marker of proliferating cells and mature neurons respectively[26,27]. Pax6 staining of the P11.5 cerebellum showed that the number of granule cell precursor cells (GCPs) in the EGL was not affected by hypoxia, while the number of migrating GCPs in the molecular layer increased, so we hypothesized that chronic hypoxia might retard the migration of GCPs (Fig. 1c). In addition, to study migration more intuitively, we performed in vivo EDU experiments in P7-P12 mice (Fig. S1b), which showed that cells in EGL and molecular layer (ML) which were double-positive for EDU and NeuN were significantly increased in the model group (Fig. S1b'). In vitro N2A cells wound-healing assays showed a significant decrease in the migration rate of cells at 12 h, 24 h, and 48 h after hypoxia (Fig. S1c). On the other side, in situ detection showed less synaptophysin (SYP) of hippocampus (Fig. 1d) and cerebellum (Fig. S1d) in mice after chronic hypoxia. Coincide with results of IF, western blotting (WB) results indicated a lower level of SYP in parallel (Fig. 1e). We also manifested that decreased expression of BDNF/TrkB signaling and Sema4F was evident in the brains of model group (Fig. 1e). What's more, we investigated the long-term effects of hypoxia in mice by SYP staining of P30 and P60 mice as well as associated protein assays. The phenotype of reduced SYP was still present in model mice at P30 (Fig. S2a) and P60 (Fig. S2c), however, the magnitude of reduction was smaller in P60 than P11.5 and P30. The expression of SYP remained down-regulated in brain tissues of the P30 (Fig. S2b) and P60 (Fig. S2d) model mice, whereas there was no change in the expression of other proteins. All these results indicated that chronic hypoxia may lead to neonatal brain disturbance by delaying migration and synaptic development in the CNS.

Chronic hypoxia alters Atoh1 levels in the developing brain

In order to further delve into the mechanism of anomalies in the development of CNS in model mice, the present study performed transcriptomic sequencing of brain tissues from the P11.5 hypoxic mice. Results showed that there were 547 differentially expressed genes (DEGs) in the model group compared with the control group (Fig. 2a). As crucial molecules in eukaryotic cell biology, TFs partake in regulating the transcription of

numerous neuron-specific genes that affect the cell cycle, excitatory neuronal differentiation, and neuronal migration[28]. Among those DEGs of the hypoxic brains, the types of TFs with altered expression were mainly focused on bHLH, Homeobox, and zf-C2H2 families (Fig. 2b). Among the differentially expressed ranked top TFs, there was a remarkable alteration in *Atoh1*, which belongs to the bHLH family (Fig. 2c). At the same time, we also verified mRNA level of *Atoh1* by RT-PCR (Fig. S3a) and observed elevated *Atoh1* levels by detecting RNA in N2A cell lines after hypoxic treatment (Fig. S3b), which was then applied as a hypoxic model in vitro. Then we isolated proteins of cytoplasm and cytoblast from P11.5 mice brains and found that the level of Atoh1 was fostered in the cytoblast compared with cytoplasmic part (Fig. 2d). These results implied that Atoh1 was involved in altering cell biological processes in the nucleus under hypoxic conditions. We then attempted to explore which neurodevelopmental processes under hypoxia that *Atoh1* was involved in. Through GO analysis of *Atoh1*, it was elicited that *Atoh1* may be in relation to neuronal migration and differentiation, and regulation of RNA polymerase II transcriptional processes (Fig. S3c). Since Atoh1 served as an important molecule in the development of cerebellar GCPs, and it has been shown that *Atoh1* expressed highly in rapidly proliferating cells, competing with other molecules to influence neuronal differentiation[29]. We examined Atoh1 in cerebellum (Fig. 2e) and hippocampus (Fig. S3d) of P11.5 mice and found that Atoh1 heighted significantly in in the model group, as well as in N2A cells in vitro (Fig. S3e). WB detection also showed that overexpression of *Atoh1* in mice brain can significantly alter protein levels of BDNF/TrkB signaling and SYP (Fig. 2f). During the differentiation of neurons, neuronal cells develop protrusions and gradually form functional synapses with others[30]. In cultured primary neurons separated from model mice, we intervened on Atoh1 levels and observed synaptic development by staining of SYP. The results showed that the number of protrusions significantly attenuated in the model+vector group compared to the control+vector group, and was further diminished after overexpression of *Atoh1* along with chronic hypoxia (model+Lenti-Atoh1) (Fig. 2g), suggesting that hypoxia as well as overexpression of *Atoh1* impeded dendritic arborization and synaptogenesis. Together, we unraveled that *Atoh1* levels altered in the developing brain and consequently delayed neuronal migration and differentiation after chronic hypoxia.

Chronic hypoxia affects brain function and causes persistent cognitive deficits in mice

Given brain maturational process delayed under neonatal hypoxia, the present study intended to investigate how the hypoxic environment with evaluation of *Atoh1* affects brain function in mice. BOLD-fMRI signals, including ReHo and ALFF, were acquired and analyzed in hypoxic mice at P60, which reflect connectivity or synchronization of regional functions and spontaneous activity of the brain, respectively[31,32]. The results demonstrated that ReHo signals altered in bilateral field CA1 of hippocampus (CA1), corpus callosum (cc), and left dorsal striatum (DS) (Fig. 3a). Moreover, ALFF of right CA1, left primary somatosensory cortex (S1), and left DS also varied in model group (Fig. 3b). Since CA1, the striatum, and somatosensory cortex play important roles in learning, memory, and execution[33–35], we intended to examine how cognitive function has been altered in hypoxic mice. Firstly, P3.5 mice were subjected to hypoxic treatment after intracerebroventricular (icv) injection of AAV2-hSyn-Atoh1-eGFP (Fig. S4a). Then we performed the open field (OF) experiment to detect the spontaneous activity and exploratory behavior of the adult mice[36]. The results showed that the time traveled in the central place was significantly sustained in the model+OE-Atoh1 group while the total distance traveled in the OF had no difference compared with that of the control+NC group, indicating that the mice might have problems with exploration rather than general locomotion (Fig. 3c). New object recognition (NOR) test was usually applied to evaluate cognitive functions through the time mice spent exploring new objects[37]. We found that in the training session, there was no difference in the sniffing time of object 1 and object 2 among the three groups, however, the mice in the control+NC group sniffed object 3 longer than the familiar one, while there was no significant tendency in the model+NC and model +OE-Atoh1 group (Fig. 3d). Next, we used the Skinner's box experiment to test reward learning and memory function in mice[38]. The results exhibited that mice in the model+NC and model+OE-Atoh1 group had fewer nose probes in the correct hole, while the model+OE-Atoh1 mice performed worst (Fig. 3e). Generally, these results manifested that chronic hypoxia altered brain function in cognition-related brain regions and continually blunted cognitive performance in mice until adulthood, which might be mediated by the abnormally excessive Atoh1.

Atoh1 affects microtubule stability by regulating Kif21b in hypoxia

Despite the present study uncovered that *Atoh1* was involved in hypoxia associated brain maturational delay and persistent cognitive dysfunction, the specific targeted signaling downstream was unknown. Further, to delve into the specific molecular mechanism of *Atoh1* involvement in this process, the downstream of the Atoh1 was screened next. A total of 11 co-altered genes were obtained by joint analysis of the datasets in GEO database[39] and the transcriptomic sequencing results of this study (Fig. 4a). After analyzing these 11 genes by KEGG and GO analysis, we hypothesized that kinesin family member 21b (*Kif21b*) may be dominantly involved in the downstream (Fig. 4a). Next, two binding sites with high relative scores of Atoh1 and *Kif21b* were predicted by the JASPAR database (Fig. 4b). The binding of Atoh1 to *Kif21b* was further verified by CHIP-PCR. Results showed that the transcriptional level of *Kif21b* was increased in N2A cells after hypoxia, and decreased when *Atoh1* was knocked down under hypoxia (Fig. 4b). WB results demonstrated that the expression of Atoh1 and Kif21b in N2A cell lines after hypoxia was significantly higher than that in the blank control group. When *Atoh1* was knocked down under hypoxia, the expression of Kif21b was decreased compared with that of the blank hypoxic group, while overexpression of *Atoh1* significantly increased the expression of Kif21b (Fig. 4c). Furthermore, we also detected a higher level of Kif21b in the brain of P11.5 model mice (Fig. 4d), implying that *Kif21b* might function as a target of Atoh1 in chronic hypoxia. After GO analysis of *Kif21b*, it was found that *Kif21b* mainly participates in biological processes such as ATP binding and hydrolysis, activation of microtubule-associated proteins, microtubule motility, and formation of cell protrusions and cytoskeleton (Fig. S5a). Accordingly, we posited that the abnormal expression of Atoh1 and Kif21b may affect the MTs-related activities and thus participated in the neurodevelopmental abnormalities caused by chronic hypoxia. IF detection of MAP2 was performed in N2A cells after hypoxia. The results indicated that expression of MAP2 was attenuated in the blank model group compared with the blank control group, uncovering that the stability of MTs within neurons was disrupted after hypoxia, while overexpression of *Atoh1* resulted in a further downregulation. In contrast, after the knockdown of *Kif21b* during overexpression of *Atoh1* under chronic hypoxia, MAP2 expression was advanced comparing with the blank model group, which was not statistically different (Fig. 4e). What's more, the wound-healing assays showed a significant effect in the migration rate of cells under manipulation of Atoh1/Kif21b signaling at 12 h, 24 h, and 48 h after hypoxia (Fig. S6a). Then after icv injection of recombinant AAV in model mice, we found similar results in cerebellum (Fig. 4f) and hippocampus (Fig. S4b), in addition, WB detection also showed that manipulation of *Atoh1* in mice brain can significantly alter protein levels of MAP2 (Fig. S4c), suggesting that knockdown of *Kif21b* might alleviate the MTs dynamic instability caused by excessive Atoh1. Additionally, we found that the effect of Atoh1 on MTs under hypoxia was still present in the hippocampus (Fig. S6b) of P30 mice but was attenuated in the cerebellum to some extent (Fig. S6c). MTs are mainly composed of α-tubulin and β-tubulin which is normally in a dynamic state[40]. Acetylated α-tubulin is a free state of α-tubulin and the ratio of acetylated-α-tubulin in total α-tubulin can reflect the stability of MTs to a certain extent[41,42]. In our study, we discovered that the acetyl/total-α-tubulin value in the N2A cell lines of the blank hypoxic group was significantly higher than that of the blank control group, and the acetyl/total-α-tubulin value was further elevated after overexpression of *Atoh1* in parallel with hypoxia. After the knockdown of *Kif21b* in hypoxia, acetyl/total values

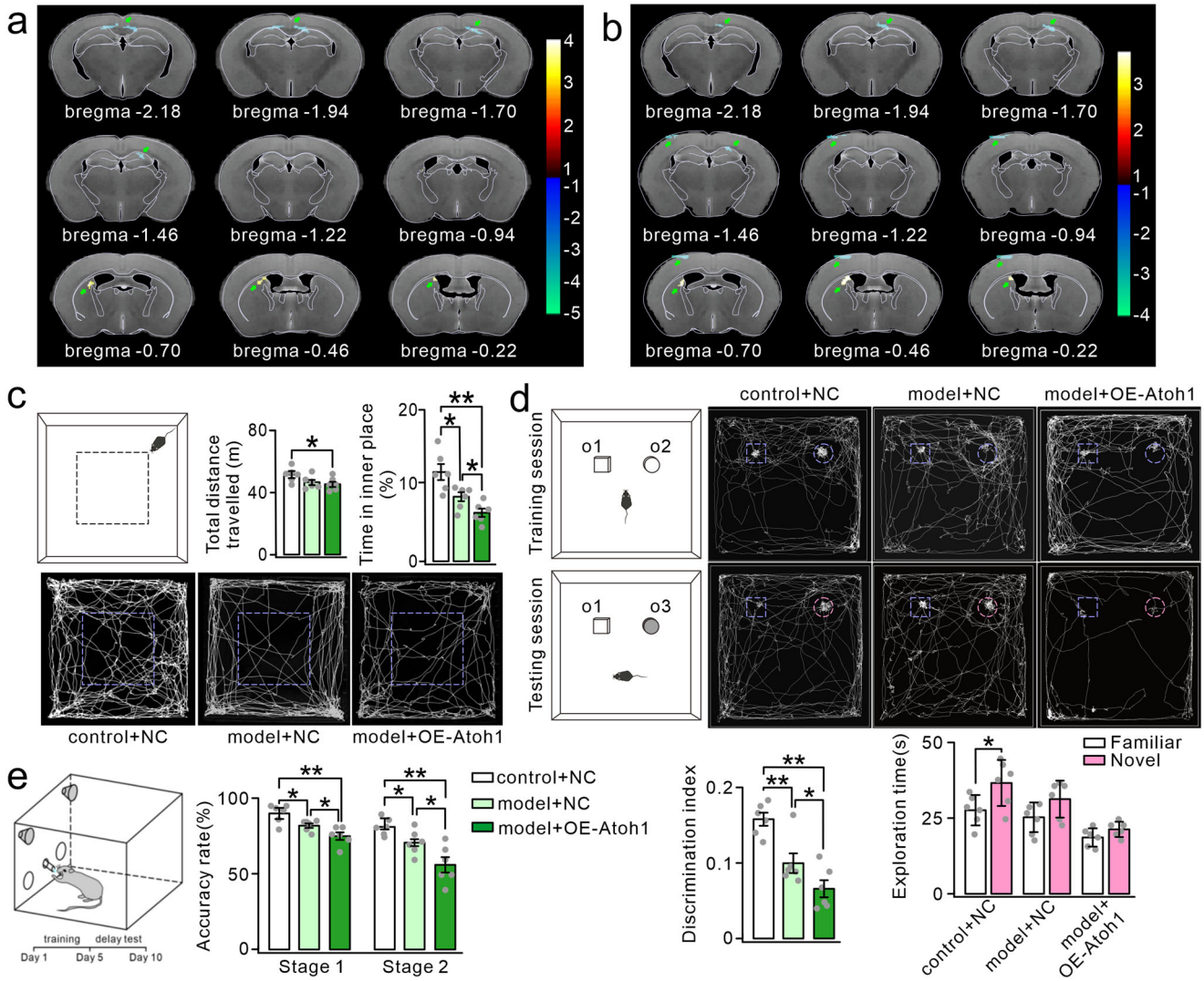

Fig. 3 | The results of resting-state BOLD and cognition-related behavior tests of model mice. a ReHo analysis of control and model mice at P60 ($p < 0.05$) (control, $n = 6$; model, $n = 6$). **b** ALFF analysis of control and model mice at P60 ($p < 0.05$) (control, $n = 6$; model, $n = 6$). The bregma for each layer of the brain map is shown below the image in the (**a**, **b**). The green arrows indicate changes of brain regions. **c** Top left: schematic of the OF tests. Top right: bar graphs show the total distance traveled in OF and time in inner space (control + NC, $n = 6$; model + NC, $n = 6$; model + OE-Atoh1, $n = 6$) (For statistics, see Table S12). Bottom: Sample tracing of mice in OF. **d** The most left panels: schematic of the NOR tests. The right three panels: Sample tracing of mice in training and testing sessions. Bar graph in bottom left panel shows the discrimination index. Bar graphs in bottom right panel show the exploration time of the familiar and novel object (control + NC, $n = 6$; model + NC, $n = 6$; model + OE-Atoh1, $n = 6$) (discrimination index, $F = 17.49$, $df = (15, 2)$ control + NC vs model + NC, $^{**}p = 0.0020$; control + NC vs model + OE-Atoh1, $^{**}p = 0.0010$; model + NC vs model + OE-Atoh1, $^{*}p = 0.049$ (0.16 ± 0.0087 vs 0.10 ± 0.013 vs 0.068 ± 0.011); exploration time, for statistics, see Table S13. **e** The left panel: schematic of the Skinner's box tests. The right panel: Bar graphs show accuracy of mice in probing the correct hole to achieve reward in the first stage and the second stage (control + NC, $n = 6$; model + NC, $n = 6$; model + OE-Atoh1, $n = 6$) (For statistics, see Table S14). All data were shown as mean ± SEM. $^{*}p < 0.05$, $^{**}p < 0.01$.

reduced comparing to the blank hypoxic group. Overexpression of *Atoh1* and knockdown of *Kif21b* after hypoxia, the acetyl/total-α-tubulin value was comparable to the model+NC group (Fig. 4g). In conclusion, these results suggested that the plethora of Atoh1 under chronic hypoxia could affect MTs' dynamic stability and consequently cause a delay in neuronal migration by modulating *Kif21b* expression.

Modulation of Atoh1 under hypoxia promotes neuronal maturation

Since we have demonstrated that the stability of neuronal MTs under hypoxia was regulated by Atoh1/Kif21b, we wanted to explore whether the regulation of *Atoh1* can promote neuronal migration and protrusion formation. Firstly, WB assays were performed in treated N2A cells. The expression of neuronal development-related proteins BDNF, TrkB, Sema4F, SYP, and p-ERK/ERK was highest in the blank control group and decreased in the blank model group, and the reduction was even more pronounced in the model+Lenti-Atoh1 group, whereas the expression of these proteins after treatment of Si-Kif21b was not significantly different from the blank model group (Fig. 5a). Next, we performed in situ staining of MAP2 in N2A cells (Fig. 5b) and mice brains (Fig. 5c) to detect MTs' stability in hypoxia after down-regulation of *Atoh1*. Results showed that MAP2 expression was improved compared with the blank model group both in vitro and in vivo. Considering that cell protrusions and synaptic structure were tightly associated with intracellular scaffolds[43], SYP was constrained under hypoxia and more so after overexpression of *Atoh1*. We performed Sholl analysis after SYP staining in the cultured primary neurons. The results showed that the blank control group had the most branches numbers, when neuronal *Atoh1* was knocked down before hypoxic

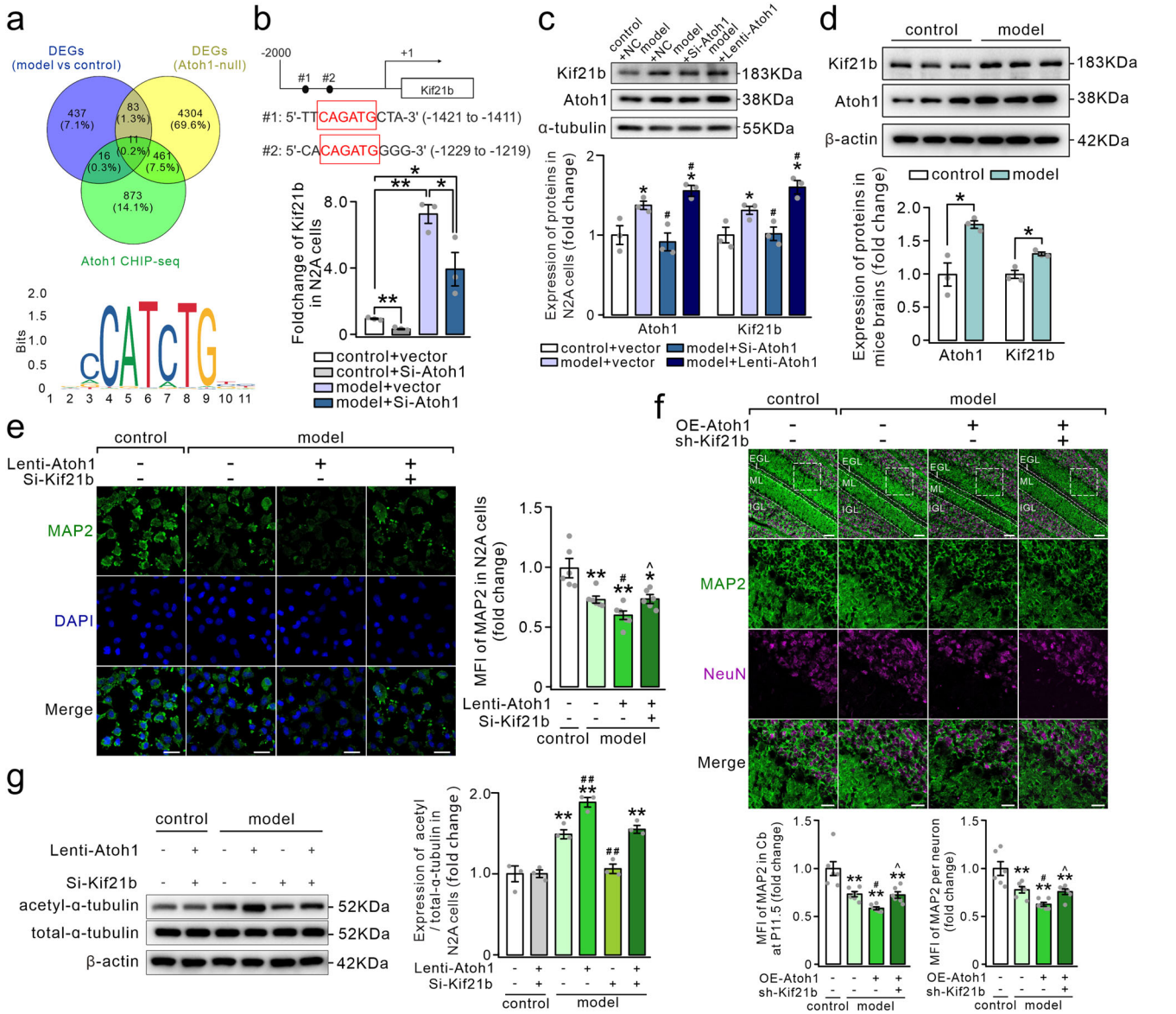

Fig. 4 | Atoh1 regulates expression of Kif21b and affects microtubule stability under hypoxia. a Upper: Venn diagram shows co-altered genes analyzed by the transcriptomics sequencing data (blue), the Atoh1-null sequence dataset (yellow), and the Atoh1-CHIP sequence dataset (green). bottom: sequence logo diagram shows a prediction of conserved motif of Atoh1. **b** Upper: Transcriptional factor binding site (TFBS) of Atoh1 predicted by the JASPAR database (relative score > 0.85). Bottom: Bar graph shows transcription of *Kif21b* by Atoh1 verified by real time-PCR in N2A cells (All groups, n = 3) (control + vector vs control + Si-Atoh1, $t = 8.54$, $^{**}p = 0.0011$, $df = 4$; model + vector vs model + Si-Atoh1, $t = 2.84$, $^{*}p = 0.047$, $df = 4$) (1.00 ± 0.07 vs 0.40 ± 0.07 vs 7.65 ± 1.14 vs 3.99 ± 1.42). **c**, Protein fractions extracted from N2A cells after transfection and hypoxia were tested with Kif21b and Atoh1. Upper panels show representative bands of proteins mentioned above. α-tubulin was used as internal control. Bar graphs show percentage changes of proteins, *p vs control + vector; #p vs model + vector (All groups, n = 3) (For statistics, see Table S15). **d** Protein fractions extracted from brains of P11.5 mice were tested with Kif21b and Atoh1. Upper panels show representative bands of proteins mentioned above. β-actin was used as internal control. Bar graphs show percentage changes of proteins relative to control (control, $n = 3$; model, $n = 3$) (For statistics, see Table S16). **e** Staining of N2A cells after transfection and hypoxia by antibody against MAP2. Scale bars: 20 μm. Objective 40x. Bar graphs show MFI of MAP2 staining, data were presented as relative changes (*p vs control+ vector; #p vs model+ vector; ^p vs model+ Lenti-Atoh1) (All groups, $n = 6$) ($F = 14.14$, $df = (20, 3)$, control + vector vs model + vector, $^{**}p = 0.0010$; control + vector vs model + Lenti-Atoh1, $^{**}p = 0.0010$; control + vector vs model + Lenti-Atoh1 + Si-Kif21b, $^{*}p = 0.010$; model + vector vs model + Lenti-Atoh1, $\#p = 0.039$; model + Lenti-Atoh1 vs model + Lenti-Atoh1 + Si-Kif21b, $\wedge p = 0.036$) (1.00 ± 0.068 vs 0.74 ± 0.028 vs 0.61 ± 0.037 vs 0.73 ± 0.030). **f** Staining of cerebellar lobule IV-V by antibodies against MAP2 and NeuN in P11.5 mice after micro-injection of recombinant virus illustrated and hypoxia. The three panels below show a magnified view of dashed squares on the top. Scale bars: 50 μm (columns above, objective 20x); 20 μm (three columns below, objective 63x). Bar graphs on the left show MFI of MAP2 staining. Bar graphs on the right show MFI of MAP2 around per neuron, data were presented as relative changes (*p vs control+NC; #p vs model+NC; ^p vs model+ OE-Atoh1) (All groups, $n = 6$) (For statistics, see Table S17). **g** Protein fractions extracted from N2A cells after transfection and hypoxia were tested with acetyl-α-tubulin and total-α-tubulin. β-actin was used as internal control. Bar graphs show percentage changes of proteins, *p vs control + vector; #p vs model + vector (All groups, $n = 3$) ($F = 35.34$, $df = (12, 5)$, vs control + vector, from left to right, $p = 0.71$, $^{**}p = 0.0010$, $^{**}p = 0.0010$, $p = 0.30$, $^{**}p = 0.0010$; vs model + vector, from left to right, $\#\#p = 0.0010$, $\#\#p = 0.0010$, $p = 0.577$) (1.00 ± 0.10 vs 1.04 ± 0.050 vs 1.56 ± 0.057 vs 1.93 ± 0.060 vs 1.10 ± 0.059 vs 1.61 ± 0.049). All data were shown as mean ± SEM. $^{*}p < 0.05$, $^{**}p < 0.01$.

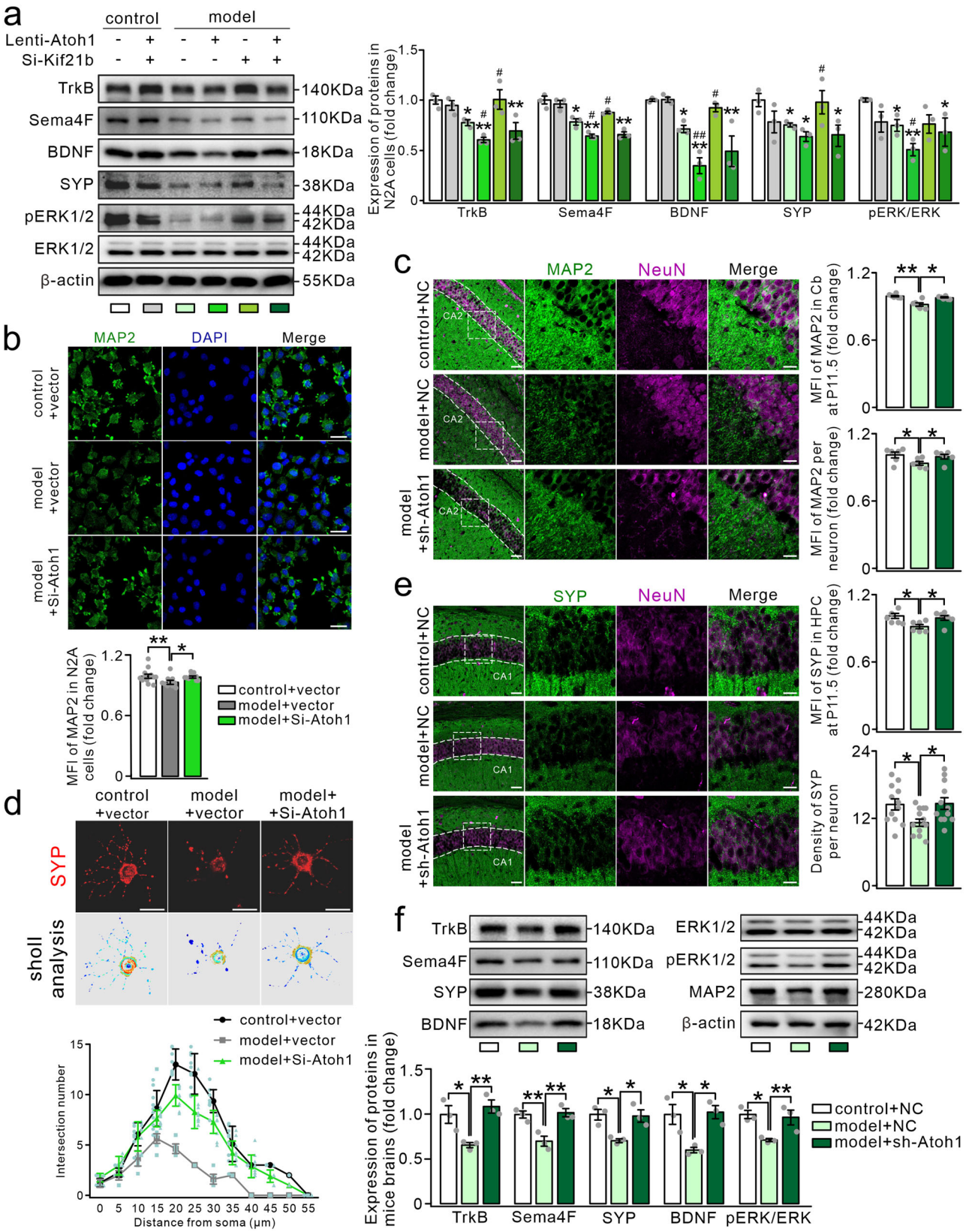

treatment, the number of dendritic branches augmented (Fig. 5d). Similarly, the restoration of MTs' dynamic stability was also verified after icv injection of AAV2-hSyn-sh-Atoh1-T2A-mcherry-WPRE in vivo (Fig. 5e). IF staining of Ki67 and NeuN in P11.5 mice indicated that the ratio of NeuN positive cells advanced in the EGL of the model+sh-Atoh1 group compared with that of the model+NC group, which was comparable to the control +NC group (Fig. S7a). Moreover, we also performed EDU experiments in vivo and cells wound-healing assays in vitro, which showed that the migration rate under hypoxia reverted after down-regulation of *Atoh1* both in GCPs (Fig. S7b) and N2A cells (Fig. S7c). After virus injection, WB assays

Fig. 5 | Downregulation of Atoh1 under hypoxia promotes MTs stability and neuronal migration. a Protein fractions extracted from N2A cells after transfection and hypoxia were tested with TrkB, BDNF, SYP, Sema4F, pErk1/2, and Erk1/2. β-actin was used as an internal control. Bar graphs show percentage changes of proteins (*vs control+ vector; #vs model+ vector) ($n = 3$ per group) (For statistics, see Table S18). **b** Staining of N2A cells after transfection and hypoxia by antibody against MAP2. Scale bars: 20 μm. Objective 40x. Bar graph shows MFI of MAP2 staining, data were presented as relative changes ($n = 6$ per groups) ($F = 4.70$, $df = (33, 2)$, control + vector vs model + vector, $^{**}p = 0.0080$; model + vector vs model + Si-Atoh1, $^{*}p = 0.020$) (1.00 ± 0.020 vs 0.94 ± 0.014 vs 0.99 ± 0.0082). **c** Staining of hippocampal CA2 by antibodies against MAP2 and NeuN in P11.5 mice after micro-injection of recombinant virus and hypoxia. The three right panels show a magnified view of dashed squares on the left. Scale bars: 50 μm (columns above, objective 20x); 20 μm (three columns below, objective 63x). Bar graph above shows MFI of MAP2 staining, data were presented as relative changes ($n = 6$ per group). Bar graph below shows MFI of MAP2 around per neuron, data were presented as relative changes ($n = 6$ per group) (For statistics, see Table S19). **d** Sholl analysis of cultured primary neurons stained by SYP after treatment illustrated. Line chart shows the intersection numbers of dendrites and concentric circles. (All groups, $n = 6$ batches for each group, $n = 2$ cells for each batch) (For statistics, see Table S20). **e** Staining of hippocampal CA1 by antibodies against SYP and NeuN in P11.5 mice after micro-injection of recombinant virus and hypoxia. The three right panels show a magnified view of dashed squares on the left. Scale bars: 50 μm (columns above, objective 20x); 20 μm (three columns below, objective 63x). Bar graph above shows MFI of SYP staining, data were presented as relative changes (For all groups, $n = 6$). Bar graph below shows density of SYP^{+} points on per neuron (For all groups, $n = 12$) (For statistics, see Table S21). **f** Protein fractions extracted from brains of P11.5 mice after hypoxia and micro-injection of recombinant virus were tested with TrkB, BDNF, SYP, Sema4F, pErk1/2, and Erk1/2. β-actin was used as an internal control. Bar graphs show percentage changes ($n = 3$ per group) (For statistics, see Table S22). All data were shown as mean ± SEM. $^{*}p < 0.05$, $^{**}p < 0.01$.

were also performed to test neuronal development-related proteins, whose levels were rescued by inference of *Atoh1* in hypoxia (Fig. 5f). In summary, the above results unveiled that microtubule stability, neuronal migration, and synapse-associated protein expression can be ameliorated by decreasing Atoh1 under chronic hypoxia.

Regulation of Atoh1/kif21b after hypoxia improves distant cognitive performance in mice

Considering that modulation of *Atoh1* after hypoxia facilitated MTs' stability and promoted neuronal migration as well as synaptic development, can cognitive ability be rescued in mice? Therefore, we examined a variety of cognitive-related behaviors in mice that were subjected to viral injection as well as hypoxia-treated. Firstly, we performed the OF test in 3 groups of mice, and the results showed that compared with the model+NC group, mice in the model+sh-Atoh1 group showed an increase in the time traveled in the inner space, which was comparable to that of the control+NC group (Fig. 6a). Next, through the NOR assays, we found that the discrimination index of the model+sh-Atoh1 group reverted to some extent compared to the model+NC group, demonstrating a tendency toward a new object (Fig. 6b). Finally, we performed Skinner's box experiments on mice. Consistent with expectations, mice in the model+sh-Atoh1 group showed a heighted correct rate of nose probing compared to the model+NC group (Fig. 6c). To observe the long-term effects of knockdown of *Atoh1* in mice, we examined brain development in P30 and P60 mice. The phenotype of reduced SYP (Fig. S8c) and MAP2 (Fig. S8d) was restored by interference of *Atoh1* in model mice at P30 in hippocampus and cerebellum, and the expression of SYP and MAP2 also reverted in WB assays at P30 in the model +sh-Atoh1 group (Fig. S8b). Moreover, we found that the expression of MAP2 in model mice at P60 was comparable with the control+NC group (Fig. 6e), but the SYP level was reinstated in both hippocampus (Fig. 6d) and cerebellum (Fig. S8a) by IF and WB (Fig. 6e) detection in the model+sh-Atoh1 group. To sum up, hypoxia-induced consistent cognitive impairment in adult mice was rescued to moderately by knocking down brain Atoh1 expression.

Discussion

Many clinical studies have demonstrated that preoperative chronic hypoxia is an important cause of neurodevelopmental deficits in children with CCHD, including delayed neuronal maturation and migration, synaptic formation and function, and myelin development etc, which consequently cause a series of functional impairments, but there are still more enormous mechanisms waiting to be explored. Here, with transcriptomic sequencing, we found that *Atoh1*, which is involved in MTs' binding, neuronal migration and differentiation, and regulation of transcriptional processes, is aberrantly expressed in a mouse model of chronic hypoxia. In hypoxic brain, Atoh1 regulated cytoskeletal stability through the modulation of Kif21b, in turn affecting cell migration and neural protrusion. In addition, by knocking down Atoh1 expression in the brain, the neurodevelopmental phenotype was restored and cognitive deficits were ameliorated in model mice. These findings may have broad implications for our understanding of the pathogenesis of chronic hypoxia-induced abnormalities in neonatal brain development and function.

Cerebral oxygen dysfunction is a typical preoperative risk factor for CCHD-associated neurodevelopmental injury[3,9], resulting in a state of constant stress in which fast-developing neuronal cells are in short supply of energy[44]. Cells have to autonomously adapt to varying oxygen levels to compensate and survive, initiating a series of signaling pathways to activate or inhibit the activity of TFs. Hence, we wanted to explore how TFs have changed under hypoxia. After analyzing the transcriptomics results of P11.5 hypoxic mice brains, we found 52 TFs with altered expression, of which the up-regulated ones were mainly focused on the bHLH family. The bHLH family regulates cell differentiation, growth, apoptosis, and metabolism, including *MyoD*, *NeuroD*, and *HIF-1α*, which served as paramount role in hypoxia[45]. After further validation by RT-PCR, we found that *Atoh1* which belongs to the bHLH family had the most obvious changes among all TFs. *Atoh1*, also known as atonal homolog 1, is mainly expressed in progenitor cells of the rhombic lip (RL) in the CNS[46]. These progenitor cells differentiate into multiple cell subtypes during development to participate in physiological processes such as respiration, locomotion, proprioception, and arousal[17,19]. It has been shown that Atoh1 can influence neuronal differentiation by participating in the regulation of the expression of genes such as *NeuroD1*, *Tubb3*, and *Gfi1*[47]. The absence or down-regulation of *Atoh1* prevents the normal development of the CNS[48]. Since Atoh1 can interact with neuronal differentiation-related genes, an abnormal increase in Atoh1 may disrupt the balance between proliferation and differentiation, resulting in neurons not being able to migrate to the appropriate region and differentiate into the designated types at the right time, which ultimately affect normal cell production and structural maintenance[20,29,49]. Migrating from the EGL to inner granular layer (IGL) is a symbol of maturation for GCPs[50], which is one of the most well-known cell migrant activities in the CNS. In our study, we found that the percentage of proliferating Ki67-positive cells in the outer EGL increased and the NeuN-positive cells in the inner EGL decreased, whereas the number of Pax6-positive cells in the EGL maintained at equal numbers in the model group, suggesting that chronic hypoxia might delay the normal migration of GCPs. The percentage of Ki67-positive cells in the EGL reverted to normal subsequently after injection of *Atoh1* interfering viruses, indicating that high expression of *Atoh1* in the neonatal brain after hypoxia hinders the normal migration and differentiation of GCPs. What's more, the results of P7 to P12 mice EDU experiments and N2A cells wound-healing assays have also indicated that the migration activity was regulated by Atoh1 under chronic hypoxia. Similar impaired migration has also been found in the cortex, where Morton et al. revealed in a model of hypoxic piglets that cortical growth is limited by slowed migration of neural stem cells from the subventricular zone to the frontal lobe and differentiation processes to interneurons[25]. It is suggested that chronic hypoxia allows for changes in the migratory activity of different regions within the CNS, and

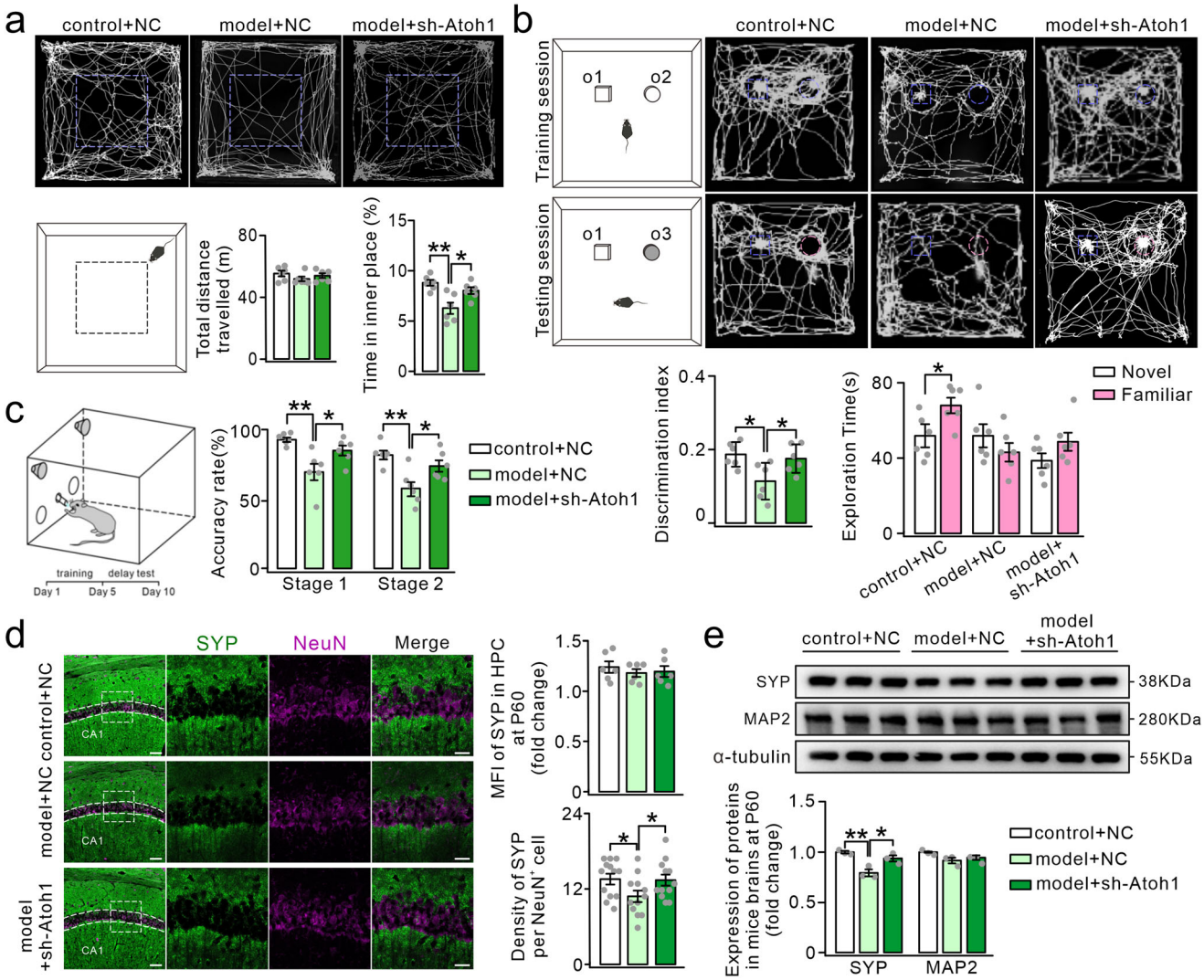

Fig. 6 | Downregulation of Atoh1/kif21b after hypoxia improves distant cognitive performance in mice. a Upper: Sample tracing of mice in OF tests after manipulation. Bottom left: Schematic of the OF tests. Bottom right: Bar graphs show the total distance traveled in OF and time in inner space ($n = 6$ per group) (For statistics, see Table S23). **b** The most left panels: Schematic of the NOR tests. The right three panels: Sample tracing of mice in training and testing sessions. Bottom left panel: Bar graph shows the discrimination index. Bottom right panel: Bar graphs show the exploration time of the familiar and novel object ($n = 6$ per group) (discrimination index, $F = 5.39$, control + NC vs model + NC, $^*p = 0.014$; control + NC vs sh-Atoh1, $p = 0.63$; model + NC vs model + sh-Atoh1, $^*p = 0.021$) (discrimination index, 0.19 ± 0.030 vs 0.12 ± 0.050 vs 0.18 ± 0.040). Exploration time, for statistics, see Table S24. **c** The left panel: Schematic of the skinner's box tests. Bar graphs show accuracy of mice in probing the correct hole in the first stage and the second stage ($n = 6$ per group) (For statistics, see Table S25). **d** Staining of hippocampal CA1 by antibodies against SYP and NeuN in mice at P60. The three right panels show a magnified view of dashed squares on the left. Scale bars: 50 μm (columns above, objective 20x); 20 μm (three columns below, objective 63x). Bar graph above shows MFI of SYP staining, data were presented as relative changes (For all groups, $n = 6$). Bar graph below shows density of SYP^+ points on per neuron (For all groups, $n = 12$) (For statistics, see Table S26). **e** Protein fractions from brains of P60 mice were tested with SYP and MAP2. Panels above show representative bands of proteins mentioned above. α-tubulin was used as an internal control. Bar graphs show percentage changes of proteins (For all groups, $n = 3$) (from left to right: SYP, $F = 13.50$, $df = (6, 2)$, $^{**}p = 0.0020$, $^*p = 0.010$, 1.00 ± 0.013 vs 0.80 ± 0.035 vs 0.95 ± 0.030; MAP2, $F = 3.16$, $df = (6, 2)$, 1.00 ± 0.015 vs 0.93 ± 0.028 vs 0.94 ± 0.022). All data were shown as mean ± SEM. $^*p < 0.05$, $^{**}p < 0.01$.

that such changes may stem from alterations in the levels of key TFs. However, those TFs identified in our chronic hypoxia model were based on a whole-brain scale. The changes in these TFs in different brain regions are still debatable, since numerous genes may be differently altered in brain regions, which weight upon more detailed studies targeting different brain regions in the future.

Meanwhile, by screening downstream molecules, we found a possible effector protein, Kif21b, which belongs to the N-terminal kinesin superfamily, and mature Kif21b is highly aggregated in dendrites[51]. On the one hand, Kif21b regulates trafficking to transport macromolecules in the distal dendrites back to the cell body for signaling transduction[52], on the other hand, Kif21b maintains the cytoskeleton homeostasis by regulating the dynamic remodeling of MTs, thus keeping the integrity of the neuron and synapse structure[53]. Through both of these aspects, Kif21b can dynamically regulate dendritic activity. Furthermore, it has been shown that abnormal elevation and decrease in Kif21b subvert the dynamic equilibrium of MTs and are associated with neuronal developmental disorders[54]. Our results manifested that excessive Atoh1 made aberrant changes in Kif21b levels, leading to an increase in acetylated α-tubulin and a disruption of MTs' kinetic equilibrium, which ultimately resulted in an impairment of intracellular cytoskeletal stability in chronic hypoxia, as shown by downregulated MAP2 in P11.5 model mice and N2A cells, which enables MTs interaction with actin filaments, thus playing a key role in the microtubule-actin network[55]. What's more, the expression of MAP2 kept lower in P30 but reverted to normal at P60 mice. We speculated that it may stem from the effect of Atoh1 on MTs' diminishes until it is restored as the hypoxic state is

lifted. BDNF has regulatory functions in neuronal growth, development, and differentiation[56], in addition to being involved in activity-dependent neuronal plasticity, regenerative repair and protection after injury, and neural network formation[57]. When BDNF binds to TrkB, the complex will be retrogradely transported by Kif21b to the nucleus and activate the relevant signaling pathways. Since decreased levels of TrkB and BDNF proteins were found in our assays of in vivo and in vitro hypoxic models, we hypothesized that Atoh1/Kif21b may act as a complement for down-regulated BDNF-TrkB level to ensure adequate intra-nuclear activation, but such compensation sacrifices its role in cytoskeletal remodeling, affecting neuronal cellular integrity as well as the maintenance of synaptic architecture. Although the reduction of Atoh1/Kif21b recovered neuronal cytoskeleton instability under hypoxic conditions in our study, the retrograde transport of proteins from distal dendrites might be affected by it, thus appropriate management of the balance between MTs stability and retrograde transport shall be more effective. Furthermore, since Atoh1/Kif21b can retrogradely carry various complexes[51], what is the role of other complexes in regulating neuronal development under hypoxic conditions? Are they beneficial or harmful? This remains to be further investigated. Atoh1 is an important TF related to growth and development in different brain regions[18–20], and there are many other downstream molecules, what molecules are also changed with the altered expression of *Atoh1*? Whether their alterations also affect the cognitive behavioral abilities of mice also requires further work to screen.

Previous studies have shown that patients with complex critical CHD have a high prevalence of cognitive deficits[5], which continue to occur in the preschool and adolescent periods[5,58]. In our past clinical studies, we found that preschool children with CCHD had significantly lower cognitive levels than normal children, and that such changes were associated with cortical thickness, white matter damage, and resting BOLD signaling[12,58], thus it appears to be urgent to clarify what changes have occurred in neonatal brain associated with cognitive deficits. Several previous studies have shown that chronic prenatal and early postnatal injury impairs the recruitment of later migrating neurons and their synaptic connectivity, as well as delays in the maturation of neurons with reduced dendrites and spines, ultimately contributing to long-term neurodevelopmental deficits in children with CHD and hypoxic mice[3,59]. In our study, mice with chronic hypoxia were found to exhibit worse performance in recognition of novel objects and lower probability of obtaining rewards in Skinner's box in adolescence as well as adulthood periods, which were similar to some of our previous clinical studies[11,12,22], suggesting that early disturbance of chronic hypoxia in neonatal brain can consistently cause functional impairment both in people and rodents. Then we identified that higher Atoh1 expression under hypoxia had an impact on cognitive behaviors over a longer period of time. Such behavioral phenotypes might arise from the delay and effects caused by Atoh1 on neuronal maturation allowing for reduced synapses, such as the reduction in SYP that we found in primary neurons, which specifically appears on presynaptic vesicle and is involved in activity-dependent-synaptic formation and vesicle endocytosis[60,61]. However, it is worth noting that model mice were in higher anxiety level in the OF behavioral experiments, and more so after overexpression of *Atoh1*. This also raised two questions for us. On the one hand, the emotional state of the mice may affect their ability of learning and memory, on the other hand, in addition to cognitive functions, the mice's sensory, emotional, and executive functions may be altered after perinatal hypoxia, thus clarifying the relationship between these behaviors will also be the focus of future exploration.

BDNF/TrkB signaling plays an indispensable role in initiating synaptogenesis and neuronal immigration by a series of downstream signaling pathways[62,63]. Sema4F is also belongs to a large family of secreted and membrane-bound proteins and interacts with postsynaptic density protein-95 (PSD95) to function in the formation of excitatory synapses[64]. Although the BDNF/TrkB signaling and Sema4F kept normal in P30 and P60 mice, reduced SYP levels persisted into adult mice in our study. We hypothesized that despite more environmental and synaptic plasticity influences continued over time, leaving P60 mice in a favorable situation, impairment of synaptic development that occurred in early life failed to improve completely. Subsequently, we improved cognition and expression of SYP to some extent in hypoxic mice by decreasing whole-brain *Atoh1* expression, suggesting that *Atoh1* may serve as a potential therapeutic target in the future. However, in this manuscript, we did not partition the brain regionally. The altered expression of *Atoh1* may be brain-wide or may be the result of alterations in particular regions, and its expressional pattern may be different in these brain regions. Henceforth, more research work is needed to refine it in the future. It is well known that the functional specificity of brain regions is the basis of behavioral diversity[65], and diverse molecules in many brain regions may undergo various changes under hypoxia due to different sensitivity to low oxygen[66–68], in addition, these molecules may also have different functions and consequently affect different behaviors. Finding specific target molecules will be the focus of future research in CHD-associated neurodevelopmental disorders. Moreover, the animal model used in this article only simulated the risk factor of preoperative hypoxia in clinical patients with CCHD. Changes in the genome will be regulated by a wider range of factors in more intricate risk conditions in the clinic, therefore more studies should be conducted together with clinical results.

Methods

Animal and Hypoxic rearing

Animals were all purchased from the Animal Core Facility of Nanjing Medical University. The experimental operation process strictly abided by the regulations of the Experimental Animal Management Committee of Nanjing Medical University. C57/BL6J mice were kept in a constant temperature of 24 °C and the light: darkness was 12 h: 12 h cycle environment for delivery. To construct an animal model for clinical CCHD-associated perinatal hypoxia in the third trimester and pre-operation, mice from postnatal day 3.5 (P3.5) to 11.5 (P11.5) were subjected to an oxygen concentration of 10.5% ± 1.0%[69,70]. Chronic hypoxia modeling was similar to previous studies[22]. Briefly, the P3.5 mouse pups and the mother mice were together kept in the hypoxic box (10.5% ± 1% FiO_2) purchased from Zhongshi Dichuang Technology (Bejing, China), and they were all returned to the standard laboratory feeding environment on P11.5 days. The pups used for experiments were all male mice. All pregnant and lactating mice were of the first three pregnancies, which have not experienced hypoxia before, and were in good health.

Cell culture and hypoxic treatment

The primary mouse neuronal cells, Neuro-2a (N2A) cells purchased from the National Collection of Authenticated Cell Cultures (Shanghai, China) was cultured in DMEM supplemented with 10% FBS, 1% penicillin/streptomycin at 37 °C with 5% CO_2 atmosphere. For the hypoxia condition, the oxygen concentration was kept at 3% for 48 h. Full names of abbreviations are detailed in Table S1.

Cell transfection

Lenti virus and double-stranded siRNAs targeting *Atoh1* and *Kif21b* were synthesized by GenePharma (Suzhou, China). Overexpressing *Atoh1* was generated using the plasmid vector VP001-CMV-MCS-3flage-EF1-ZsGreen-T2A-PURO. Briefly, we resuscitated and passaged N2A cells and laid them on a 6-well plate. When the cell density reached 60-70%, the cells were transfected with Lipofectamine 2000 (Invitrogen, CA, USA). Transfected cells were cultured for one day and then treated with hypoxia or normoxia. Sequences of siRNAs are detailed in Table S2.

Wound-healing assays

When the N2A cell density reached approximately 90%, the cultured cells were scratched using a 1 ml pipette tip within the confines of a straightedge. After completing the cell scratching, the cells were washed with PBS to remove floating cells, and then low serum medium containing antibiotics was added to culture the cells. Image data of cell migration was collected after 0 h, 12 h, 24 h, and 48 h of scratching. Full names of abbreviations are detailed in Table S1.

Chromatin Immunoprecipitation (CHIP)

CHIP kit purchased from GZSCBIO (Guangzhou, China) was used in this experiment. Briefly, when the cell density reached 3–4 × 10^6 per well, 1% PFA was added, and glycine was used to stop cellular cross-linking. After rinsing with PBS on ice, the cell suspension was transferred into an EP tube. Lysates were subjected to centrifugation after treatment by cell lysis buffer, and then MNase digestion buffer was used to break chromosomes. To detect chromatin breakage, we added 90 μL Elution buffer to 10 μL of the sample and then incubated it at 65 °C for 2 h and added 2 μL of proteinase K. After 1 h of incubation, DNA was extracted for agarose gel electrophoresis. For antibody incubation, each tube contained 100 μL of sample and 900 μL of CHIP buffer. In addition, 10 μL of each set of samples was taken as an input and stored at −20 °C. After that, the antibodies were added according to the group and incubated overnight at 4 °C with rotation. After the incubation was completed, the overnight incubated antibody-chromatin complex was added to the washed beads and incubated for 4–6 h at 4 °C with rotation. The complexes were then washed with CHIP buffer, Low salt buffer, High salt buffer, LiCl buffer, and TE buffer in that order. Elution buffer was then added to the input and IP groups for elution. After 1 repetition, NaCl was added and incubated at 65 °C for 2 h for de-crosslinking. After completion of the de-crosslinking, DNA was extracted using phenol-chloroform and prepared for PCR. Full names of abbreviations are detailed in Table S1.

Animal MRI

For this study, we used a 9.4 T BioSpec 94/20 USR MRI (Bruker, Mass, USA) to perform MRI scans of the mouse brain as previous study[22]. Briefly, while 2–3% isoflurane was used to induce anesthesia, 0.5–1% isoflurane by inhalation and 0.5 mL/10 g/h of dextromethorphan intraperitoneally were used to maintain anesthesia in scans. The upper teeth of the mice were hooked by ring gouges, and the head was secured on both sides using ear clips to ensure that the coil fits the head. A pressure transducer was placed on the chest and abdomen of the mice to observe the respiratory status of the mice. Scanning was started when the mice's respiration was maintained at a frequency of 100 breaths/min. Parameters of scans are as follows: we used RARE sequence for T2-weighted scanning, TE = 33 ms; TR = 4000 ms; NA = 5; ES = 11 ms RARE factor = 8; slices = 23 (P11.5) or 34 (P30); slice thickness = 0.5 mm; image size = 175 × 175; field of view = 14 mm × 14 mm. The sequence used for the BOLD fMRI scanning is EPI sequence, TE = 7.88 ms; TR = 1500 ms; NA = 1; repetitions = 200; signal type = fid; bandwidth = 500,000 Hz; slices = 23 (P11.5) or 34 (P30); slice thickness = 0.5 mm; image size = 110 × 48; field of view = 27.5 mm × 12 mm. In order to perform T2 analysis, the volume of total brain was manually drawn, and estimated region of interest (ROI) using 3D-slicer software (NIH, MD, USA). For BOLD analysis, we analyzed the data using SPM 12 (FIL, UK, London) based on MATLAB 2021b (MathWorks, Mass, USA) platform after converting the data to nii format using dcm2niigui (MRIcron, NITRC, USA) software. The images were first preprocessed using spmAnimalIHEP for temporal correction, spatial correction, alignment, and segmentation. Then the adaptive templates were made after removing the highlighted pixels outside the brain using ITKSNAP software (NC, USA). Finally, it was used as an analysis template, and unpaired two sample t-test analysis was performed on preprocessed data to obtain the regional homogeneity (ReHo) and amplitude of low-frequency fluctuation (ALFF) results. Full names of abbreviations are detailed in Table S1.

Recombinant virus and in vivo injection

AAV2-hSyn-Atoh1-T2A-GFP-WPRE, AAV2-hSyn-sh-Atoh1-T2A-mcherry-WPRE, and AAV2-hSyn-sh-Kif21b-T2A-mcherry-WPRE viruses were obtained from General Biol (Anhui, China). Briefly, mice (P0) were firstly anesthetized in a freezer for 3–4 min and quickly fixed on a stereotaxic equipment (RWD, Shenzhen, China). viruses were injected into cerebroventricular at a rate of 20 nL/min using a microinjector (Hamilton, Timis, Romania). During the operation, isoflurane was used to maintain anesthesia (0.3%). After the injection was completed, pups were rapidly rewarmed using a heating blanket and returned to their mothers[71]. For coordination, bilaterally 2/5 division of the line between lambda and eyes. Behavioral experiments were preformed after 50 days of virus injection and hypoxia treatment. Full names of abbreviations are detailed in Table S1.

Animal behavior

All mice used in the behavioral experiments were males. Before all behavioral experiments, mice were handled 15 min daily for 3 days. After each test of single mouse, apparatus was cleaned by 75% alcohol. The experimental environment was kept quiet.

Open field (OF): OF testing was conducted in a 50 cm × 50 cm square box whose bottom is white for 10 min, and each mouse was placed in the center of the apparatus. After that, Fiji was used to statistically analyze the mice's movement distance, average speed of movement, and residence time in the outer and inner areas.

New object recognition (NOR): In the adaptation stage, each mouse was placed in a rectangular (50 cm × 50 cm) apparatus with a white bottom for 10 min to move freely. In the familiarization stage, two identical objects were placed in the device and each mouse was placed in the center of the device and allowed to explore freely for 10 min. Five hours after the end of the familiarization stage, one object was replaced with a new object. The mice were placed in the device to explore for 10 min. Traces were recorded and statistically analyzed by software. Sniffing time of each object was manually counted by two researchers who were blind to the tests. The ratio of (o3 − o2) to (o3 + o2) was measured as the discrimination index.

Skinner's box: Training and testing were carried out in a 30 cm × 30 cm × 30 cm Skinner's box module (Zhongshi Dichuang Technology, Bejing, China) which was equipped with two holes, corresponding lights, and flow outlets. If the mouse probed the hole correctly, the corresponding light would light up and 5% sucrose would flow out. The Skinner's box module was placed in a dark chamber of 90 cm × 55 cm × 60 cm. After fasting for 24 h before the experiment, the P60 mice were placed in Skinner's box and the test took 30 min. The tests were divided into two stages. In the first stage, the light would light up and the 5% sucrose flowed out upon the correct probe at once. In the second stage, the light could only be on and the 5% sucrose flowed out when the mice probed the correct hole for 3 s/5 s/7 s. The software recorded the number of probes in each hole and reward.

Immunoblotting

Animals were euthanized with intraperitoneal injection of 0.7% sodium pentobarbital (10 mL/kg) after induced isoflurane anesthesia. Mouse brain tissue was extracted, isolated, and lysed under ice in RIPA with protease inhibitor and phosphatase inhibitor (Beyotime, Shanghai, China), centrifuged at 10,000 rcf, 4 °C for 15 min, supernatant was collected, and protein concentrations were detected with a BCA kit. What's more, Nuclear and Cytoplasmic Protein Extraction Kit (Beyotime, Shanghai, China) was used for the extraction of protein fractions. Proteins were isolated on 8%, 12.5%, and 15% SDS-PAGE gel, and after completing the transmembrane the PVDF membrane was blocked using 5% BSA and incubated with primary antibody overnight at 4 °C. The primary antibody was washed with TBST on a secondary day, and then incubated with the secondary antibody for 1 h at room temperature. After being washed with TBST, proteins were tested with ECL kit (NCM Biotech, Suzhou, China) and data were recorded by ChemiDoc (Bio-Rad, CA, USA). Full names of abbreviations are detailed in Table S1. Information and dilutions of antibodies are detailed in Table S2.

Immunofluorescence

For staining of brain tissue, the mice were firstly induced anesthetized using isoflurane, and when the mice were in a nonconscious state, an intraperitoneal injection of 0.7% sodium pentobarbital (10 mL/ kg) was performed. The operation of perfusion started while the mice had no toe-clamping response. The reagents used in order were 0.01 M PBS and then 4% PFA (Servicebio, Wuhan, China). Tissues were fixed overnight at 4 °C and dehydrated with 30% sucrose. Frozen sections were made into 20 μm by NX-50 (Thermo, Mass, USA). After blocked and permeabilized by 10%

BSA, 1% NGS and 0.3% Triton X-100 for 1 h at room temperature, sections were incubated with primary antibodies overnight at 4 °C. After washing out the primary antibodies with PBS, sections were incubated with secondary antibodies at room temperature for 2 h. After rinsing with PBS, sections were stained with DAPI. For cell staining, after discarding the medium, cell slides were rinsed with PBS, and then fixed by 4% PFA at room temperature. After washing with PBS three times, cells were blocked for 30 min at room temperature, and then followed the protocols mentioned above. Images of sections were captured using a Zeiss lsm 700 (Zeiss, Oberkochen, German) or an Olympus BX53 (Olympus, Tokyo, Japan) microscope. Information of objectives were as follows, EC Plan-Neofluar 20x/0.50 M27, EC Plan-Neofluar 40x/0.75 M27, and Plan-Apochromat 63x/1.40 Oil DIC M27. Exposure and resolution settings were the same for all groups of the same IF experiment. The PPI of images are 512 × 512 pixels or 1024 × 1024 pixels. Fluorescent images from the same comparison experiment all had the same staining conditions and imaging parameters. The 16-bit images from the CCD were loaded into the Fiji software, and for images that required ROI selection, they were first outlined using the ROI Manager; then the images were signal selected and corrected by the Threshold function (the same thresholding algorithm was used for the same set of images rather than manually, in order to eliminate errors caused manually by different photos), and then the mean fluorescence intensity was output using the Measure window. Full names of abbreviations are detailed in Table S1. Information and dilutions of antibodies are detailed in Table S2.

EDU labeling

Each group of mice was injected with 50 mg/kg of EDU intraperitoneally at P7 and observed at P11.5. After obtaining frozen sections, NeuN antibody was used for primary and secondary antibody staining followed by EDU staining using BeyoClick™ EdU Cell Proliferation Kit with Alexa Fluor 488 (Beyotime, Shanghai, China).

Real-time PCR

Mouse brain tissue was extracted, isolated, and lysed on ice in Trizol. Then trichloromethane was added to isolate the RNA. The mix was centrifuged at 4 °C at 12,000 rcf for 15 min, after that supernatant was transferred into a new EP tube and mixed with the same volume of isopropanol. To get more RNA product, we put the mixture at 4 °C overnight. The next day after centrifugation to obtain the precipitate, it was washed with 75% ethanol and solubilized with DEPC water, the concentration was measured using one-drop (WINGS, Nanjing, China). For cells, the medium was discarded first. Then after rinsing the cells with PBS, Trizol was added to each well on ice. Cells were scraped and transferred into a 1.5 mL centrifuge tube. Followed protocols are the same as above mentioned. Before real-time PCR, RNA was reverse-transcribed into cDNA. We carried out RT-PCR in a 40 μL reaction system with a LightCycler ® 96 (Roche, Basel, Switzerland). Full names of abbreviations are detailed in Table S1.

Statistical analysis

Experiments were performed in more than three biological replicates as well as three methodological replicates respectively, as shown by individuals in bar graphs. All of data analyses were blinding, with a mixture of single and double blinding for immunoblotting, immunofluorescence, animal MRI and behavioral tests, etc. We used SPSS 22.0 (IBM Inc., USA) software for data analysis. Normality of the sample data were tested before analysis. Continuous variables were expressed as mean ± SEM. Unpaired two-sample t-tests were used to compare the differences between the two groups and one-way ANOVA was used for multiple comparisons. $P < 0.05$ was considered a significant difference. WB and IF data were analyzed by Fiji (NIH, MD, USA). We used GraphPad Prism to visualize statistics and plot them (GraphPad Software, CA, USA).

Data availability

All relevant data in this manuscript are available from the corresponding author (Xu-ming Mo and Si-yu Ma) upon reasonable request. The sequencing data was uploaded in a public website as followed. https://pan.baidu.com/s/1AmFvCi-WVg7SRCNBTthofA?pwd=kd4o. The access code is: kd4o.

Received: 12 January 2024; Accepted: 4 September 2024;
Published online: 11 September 2024

References

1. van der Bom, T. et al. The changing epidemiology of congenital heart disease. *Nat. Rev. Cardiol.* **8**, 50–60 (2011).
2. Ortinau, C. et al. Cortical folding is altered before surgery in infants with congenital heart disease. *J. Pediatr.* **163**, 1507–1510 (2013).
3. Morton, P. D., Ishibashi, N. & Jonas, R. A. Neurodevelopmental abnormalities and congenital heart disease insights into altered brain maturation. *Circ. Res*. **120**, 960–977 (2017).
4. Warnes, C. A. et al. Task force 1: the changing profile of congenital heart disease in adult life. *J. Am. Coll. Cardiol.* **37**, 1170–1175 (2001).
5. Naef, N. et al. Neurodevelopmental profiles of children with congenital heart disease at school age. *J. Pediatr.* **188**, 75–81 (2017).
6. Cassidy, A. R., White, M. T., DeMaso, D. R., Newburger, J. W. & Bellinger, D. C. Executive function in children and adolescents with critical cyanotic congenital heart disease. *J. Int Neuropsychol. Soc.* **21**, 34–49 (2015).
7. Cohen, S. & Earing, M. G. Neurocognitive impairment and its long-term impact on adults with congenital heart disease. *Prog. Cardiovasc. Dis.* **61**, 287–293 (2018).
8. Sun, L. Q. et al. Reduced fetal cerebral oxygen consumption is associated with smaller brain size in fetuses with congenital heart disease. *Circulation* **131**, 1313–1323 (2015).
9. Kelly, C. J. et al. Abnormal microstructural development of the cerebral cortex in neonates with congenital heart disease is associated with impaired cerebral oxygen delivery. *J. Am. Heart Assoc.* **8**, e009893 (2019).
10. Rudolph, A. M. Impaired cerebral development in fetuses with congenital cardiovascular malformations: Is it the result of inadequate glucose supply? *Pediatr. Res*. **80**, 172–177 (2016).
11. Ma, S. et al. Changes in cortical thickness are associated with cognitive ability in postoperative school-aged children with tetralogy of fallot. *Front Neurol.* **11**, 691 (2020).
12. Ma, S. et al. The effect of abnormal regional homogeneity and spontaneous low-frequency brain activity on lower cognitive ability: a cross-sectional study on postoperative children with tetralogy of fallot. *Front Neurosci.* **15**, 685372 (2021).
13. Yang, Y. et al. Salvianolic acid A relieves cognitive disorder after chronic cerebral ischemia: Involvement of Drd2/Cryab/NF-κB pathway. *Pharm. Res.* **175**, 105989 (2022).
14. Kietzmann, T., Knabe, W. & Schmidt-Kastne, R. Hypoxia and hypoxia-inducible factor modulated gene expression in brain: involvement in neuroprotection and cell death. *Eur. Arch. Psychiatry Clin. Neurosci.* **251**, 170–178 (2001).
15. Wang, V. Y., Rose, M. F. & Zoghbi, H. Y. Math1 expression redefines the rhombic lip derivatives and reveals novel lineages within the brainstem and cerebellum. *Neuron* **48**, 31–43 (2005).
16. Lumpkin, E. A. et al. Math1-driven GFP expression in the developing nervous system of transgenic mice. *Gene Expr. Patterns* **3**, 389–395 (2003).
17. Huang, W. H. et al. Atoh1 governs the migration of postmitotic neurons that shape respiratory effectiveness at birth and chemoresponsiveness in adulthood. *Neuron* **75**, 799–809 (2012).
18. Wu, S. R. et al. Atoh1 drives the heterogeneity of the pontine nuclei neurons and promotes their differentiation. *Sci. Adv.* **9**, eadg1671 (2023).
19. Xie, W. R. et al. An Atoh1-s193a phospho-mutant allele causes hearing deficits and motor impairment. *J. Neurosci.* **37**, 8583–8594 (2017).

20. Chang, C. H. et al. Atoh1 controls primary cilia formation to allow for shh-triggered granule neuron progenitor proliferation. *Dev. Cell* **48**, 184–199 (2019).
21. Liu, G. et al. Benefits of progesterone on brain immaturity and white matter injury induced by chronic hypoxia in neonatal rats. *J. Thorac. Cardiovasc Surg.* **160**, e55–e66 (2020).
22. Ma, S. et al. Preoperative serum cortisone levels are associated with cognition in preschool-aged children with tetralogy of Fallot after corrective surgery: new evidence from human populations and mice. *World J. Pediatr.* **20**, 173–184 (2024).
23. Mills, K. I. et al. Nutritional considerations for the neonate with congenital heart disease. *Pediatrics* **49**, 1–51 (2022).
24. Paredes, M. F. et al. Extensive migration of young neurons into the infant human frontal lobe. *Science* **354**, aaf7073 (2016).
25. Morton, P. D. et al. Abnormal neurogenesis and cortical growth in congenital heart disease. *Sci. Transl. Med.* **9**, eaah7029 (2017).
26. Gerdes, J., Schwab, U., Lemke, H. & Stein, H. Production of a mouse monoclonal antibody reactive with a human nuclear antigen associated with cell proliferation. *Int J. Cancer* **31**, 13–20 (1983).
27. Duan, W. et al. Novel insights into neun: from neuronal marker to splicing regulator. *Mol. Neurobiol.* **53**, 1637–1647 (2016).
28. Cave, C. & Sockanathan, S. Transcription factor mechanisms guiding motor neuron differentiation and diversification. *Curr. Opin. Neurobiol.* **53**, 1–7 (2018).
29. Ayrault, O. et al. Atoh1 inhibits neuronal differentiation and collaborates with Gli1 to generate medulloblastoma-initiating cells. *Cancer Res.* **70**, 5618–5627 (2010).
30. Sanes, J. R. & Zipursky, S. L. Synaptic specificity, recognition molecules, and assembly of neural circuits. *Cell* **181**, 536–556 (2020).
31. Kiviniemi, V., Kantola, J. H., Jauhiainen, J. & Tervonen, O. Comparison of methods for detecting nondeterministic BOLD fluctuation in fMRI. *Magn. Reson Imaging* **22**, 197–203 (2004).
32. Tamura, Y. et al. Facilitation of A[delta]-fiber-mediated acute pain by repetitive transcranial magnetic stimulation. *Neurology* **62**, 2176–2181 (2004).
33. Eichenbaum, H. On the Integration of Space, Time, and Memory. *Neuron* **95**, 1007–1018 (2017).
34. Balleine, B. W., Delgado, M. R. & Hikosaka, O. On the integration of space, time, and memory. *J. Neurosci.* **27**, 8161–8165 (2007).
35. Romo, R., Lemus, L. & de Lafuente, V. Sense, memory, and decision-making in the somatosensory cortical network. *Curr. Opin. Neurobiol.* **22**, 914–919 (2012).
36. Garofalo, S. et al. Natural killer cells and innate lymphoid cells 1 tune anxiety-like behavior and memory in mice via interferon-γ and acetylcholine. *Nat. Commun.* **14**, 3103 (2023).
37. Leger, M. et al. Object recognition test in mice. *Nat. Protoc.* **8**, 2531–2537 (2013).
38. Hasan, M. T. et al. Role of motor cortex NMDA receptors in learning-dependent synaptic plasticity of behaving mice. *Nat. Commun.* **4**, 2258 (2013).
39. Klisch, T. J. et al. In vivo Atoh1 targetome reveals how a proneural transcription factor regulates cerebellar development [Data set]. *Proc. Natl Acad. Sci. USA* **108**, 3288–3293 (2011).
40. Gudimchuk, N. B. & McIntosh, J. R. Regulation of microtubule dynamics, mechanics and function through the growing tip. *Nat. Rev. Mol. Cell Biol.* **22**, 777–795 (2021).
41. Saunders, H. A. J. et al. Acetylated α-tubulin K394 regulates microtubule stability to shape the growth of axon terminals. *Curr. Biol.* **32**, 614–630.e5 (2022).
42. Janke, C. & Magiera, M. M. The tubulin code and its role in controlling microtubule properties and functions. *Nat. Rev. Mol. Cell Biol.* **21**, 307–326 (2020).
43. Choquet, D. & Triller, A. The dynamic synapse. *Neuron* **80**, 691–703 (2013).
44. Limperopoulos, C. et al. Brain volume and metabolism in fetuses with congenital heart disease: evaluation with quantitative magnetic resonance imaging and spectroscopy. *Circulation* **121**, 26–33 (2010).
45. Zhao, Y. Hypoxia-induced signaling in the cardiovascular system: pathogenesis and therapeutic targets. *Signal Transduct. Target Ther.* **8**, 431 (2012).
46. Machold, R. & Fishell, G. Math1 is expressed in temporally discrete pools of cerebellar rhombic-lip neural progenitors. *Neuron* **48**, 17–24 (2005).
47. Elliott, K. L., Pavlínková, G., Chizhikov, V. V., Yamoah, E. N. & Fritzsch, B. Development in the mammalian auditory system depends on transcription factors. *Int J. Mol. Sci.* **22**, 4189 (2021).
48. Flora, A., Klisch, T. J., Schuster, G. & Zoghbi, H. Y. Deletion of Atoh1 disrupts Sonic Hedgehog signaling in the developing cerebellum and prevents medulloblastoma. *Science* **326**, 1424–1427 (2009).
49. Helms, A. W., Gowan, K., Abney, A., Savage, T. & Johnson, J. E. Overexpression of MATH1 disrupts the coordination of neural differentiation in cerebellum development. *Mol. Cell Neurosci.* **17**, 671–682 (2001).
50. Consalez, G. G., Goldowitz, D., Casoni, F. & Hawkes, R. Origins, development, and compartmentation of the granule cells of the cerebellum. *Front. Neural. Circuits* **14**, 611841 (2021).
51. Marszalek, J. R., Weiner, J. A., Farlow, S. J., Chun, J. & Goldstein, L. S. Novel dendritic kinesin sorting identified by different process targeting of two related kinesins: KIF21A and KIF21B. *J. Cell Biol.* **145**, 469–479 (1999).
52. Ghiretti, A. E. et al. Activity-dependent regulation of distinct transport and cytoskeletal remodeling functions of the dendritic kinesin KIF21B. *Neuron* **92**, 857–872 (2016).
53. Muhia, M. et al. The kinesin KIF21B regulates microtubule dynamics and is essential for neuronal morphology, synapse function, and learning and memory. *Cell Rep.* **15**, 968–977 (2016).
54. Asselin, L. et al. Mutations in the kif21b kinesin gene cause neurodevelopmental disorders through imbalanced canonical motor activity. *Nat. Commun.* **11**, 2441 (2020).
55. Dehmelt, L. & Halpain, S. The MAP2/Tau family of microtubule-associated proteins. *Genome Biol.* **6**, 204 (2005).
56. Park, H. & Poo, M. M. Neurotrophin regulation of neural circuit development and function. *Nat. Rev. Neurosci.* **14**, 7–23 (2013).
57. Camuso, S., La Rosa, P., Fiorenza, M. T. & Canterini, S. Pleiotropic effects of BDNF on the cerebellum and hippocampus: Implications for neurodevelopmental disorders. *Neurobiol. Dis.* **163**, 105606 (2022).
58. Yang, M. et al. Altered brain structure in preschool-aged children with tetralogy of Fallot. *Pediatr. Res.* **93**, 1321–1327 (2023).
59. Kelly, C. J. et al. Impaired development of the cerebral cortex in infants with congenital heart disease is correlated to reduced cerebral oxygen delivery. *Sci. Rep.* **7**, 15088 (2017).
60. Kwon, S. E. & Chapman, E. R. Synaptophysin regulates the kinetics of synaptic vesicle endocytosis in central neurons. *Neuron* **70**, 847–854 (2011).
61. Tarsa, L. & Goda, Y. Synaptophysin regulates activity-dependent synapse formation in cultured hippocampal neurons. *Proc. Natl. Acad. Sci. USA* **99**, 1012–1016 (2002).
62. Wang, C. S., Kavalali, E. T. & Monteggia, L. M. BDNF signaling in context: from synaptic regulation to psychiatric disorders. *Cell* **185**, 62–76 (2022).
63. Colucci-D'Amato, L., Speranza, L. & Volpicelli, F. Neurotrophic factor BDNF, physiological functions and therapeutic potential in depression, neurodegeneration and brain cancer. *Int J. Mol. Sci.* **21**, 7777 (2020).
64. Schultze, W. et al. Semaphorin4F interacts with the synapse-associated protein SAP90/PSD-95. *J. Neurochem.* **78**, 482–489 (2001).
65. Genon, S., Reid, A., Langner, R., Amunts, K. & Eickhoff, S. B. How to characterize the function of a brain region. *Trends Cogn. Sci.* **22**, 350–364 (2018).

66. Nyakas, C., Buwalda, B. & Luiten, P. G. Hypoxia and brain development. *Prog. Neurobiol.* **49**, 1–51 (1996).
67. Miller, S. P. & Ferriero, D. M. From selective vulnerability to connectivity: insights from newborn brain imaging. *Trends Neurosci.* **32**, 496–505 (2009).
68. Back, S. A. et al. Selective vulnerability of late oligodendrocyte progenitors to hypoxia-ischemia. *J. Neurosci.* **22**, 455–463 (2002).
69. Forbes, T. A. et al. Environmental enrichment ameliorates perinatal brain injury and promotes functional white matter recovery. *Nat. Commun.* **11**, 964 (2020).
70. Semple, B. D., Blomgren, K., Gimlin, K., Ferriero, D. M. & Noble-Haeusslein, L. J. Brain development in rodents and humans: Identifying benchmarks of maturation and vulnerability to injury across species. *Prog. Neurobiol.* **106-107**, 1–16 (2013).
71. Zhou, L. et al. A patient-derived mutation of epilepsy-linked LGI1 increases seizure susceptibility through regulating Kv1.1. *Cell Biosci.* **13**, 34 (2023).

Acknowledgements

This work was supported by grants from the National Natural Science Foundation of China (82270310), the postdoctoral start-up funds of Children's Hospital of Nanjing Medical University (QDJJ2022006, QDJJ2023002, QDJJ2024003), the National Natural Science Foundation cultivation program of Children's Hospital of Nanjing Medical University (QNPY2024007, QNPY2024010).

Author contributions

Conceptualization: X.-Y.C., S.-Y.M., and X.-M.M. Methodology: X.-Y.C., and S.-Y.M. Investigation: M.-H.T., and L.H. Visualization: X.-Y.C., S.-Y.M., and M.-H.T. Supervision: X.-Y.C., S.-Y.M., L.H., K.-D.W., Z.Z., Y.-Q.Z., Y.L., and Z.-C.Y. Writing—original draft: X.-Y.C. and M.-H.T. Writing—review & editing: X.-Y.C., S.-Y.M., N.P., M.-H.T., and X.-M.M.

Competing interests

The authors declare no competing interests.

Additional information

Supplementary information The online version contains supplementary material available at https://doi.org/10.1038/s42003-024-06846-7.

Correspondence and requests for materials should be addressed to Si-yu Ma or Xu-ming Mo.

Peer review information *Communications Biology* thanks the anonymous reviewers for their contribution to the peer review of this work. Primary Handling Editor: Benjamin Bessieres.